Spectroscopic polarization-sensitive full-field optical coherence microscopy

Arnaud Dubois

Spectroscopic polarization-sensitive full-field optical coherence tomography

Arnaud Dubois*

Laboratoire Charles Fabry, Institut d'Optique, CNRS UMR 8501, Univ Paris-Sud, 2 avenue Augustin Fresnel, 91127 Palaiseau, France

**arnaud.dubois@institutoptique.fr*

Abstract: Full-field optical coherence tomography (FF-OCT) is a recent optical imaging technology based on low-coherence interference microscopy for imaging of semi-transparent samples with ~1 µm spatial resolution. FF-OCT produces *en-face* tomographic images obtained by arithmetic combination of interferometric images acquired by an array camera. In this paper, we demonstrate a unique multimodal FF-OCT system, capable of measuring simultaneously the intensity, the power spectrum and the phase-retardation of light backscattered by the sample being imaged. Compared to conventional FF-OCT, this multimodal system provides enhanced imaging contrasts at the price of a moderate increase in experimental complexity and cost.

OCIS codes: (180.1655) Coherence tomography; (180.3170) Interference microscopy; (170.4500) Optical coherence tomography; (120.6200) Spectrometers and spectroscopic instrumentation; (120.5410) Polarimetry.

References and links

1. D. Huang, E. A. Swanson, C. P. Lin, J. S. Schuman, W. G. Stinson, W. Chang, M. R. Hee, T. Flotte, K. Gregory, C. A. Puliafito, and J. G. Fujimoto, "Optical coherence tomography," Science **254**(5035), 1178–1181 (1991).
2. A. F. Fercher, "Optical coherence tomography," J. Biomed. Opt. **1**(2), 157–173 (1996).
3. E. A. Swanson, J. A. Izatt, M. R. Hee, D. Huang, C. P. Lin, J. S. Schuman, C. A. Puliafito, and J. G. Fujimoto, "In-vivo retinal imaging by optical coherence tomography," Opt. Lett. **18**(21), 1864–1866 (1993).
4. M. Wojtkowski, R. Leitgeb, A. Kowalczyk, T. Bajraszewski, and A. F. Fercher, "In-vivo human retinal imaging by Fourier domain optical coherence tomography," J. Biomed. Opt. **7**(3), 457–463 (2002).
5. J. G. Fujimoto, "Optical coherence tomography for ultrahigh resolution in vivo imaging," Nat. Biotechnol. **21**(11), 1361–1367 (2003).
6. K. Wiesauer, M. Pircher, E. Götzinger, S. Bauer, R. Engelke, G. Ahrens, G. Grützner, C. Hitzenberger, and D. Stifter, "En-face scanning optical coherence tomography with ultra-high resolution for material investigation," Opt. Express **13**(3), 1015–1024 (2005).
7. X. J. Wang, T. E. Milner, and J. S. Nelson, "Characterization of fluid flow velocity by optical Doppler tomography," Opt. Lett. **20**(11), 1337–1339 (1995).
8. J. A. Izatt, M. D. Kulkarni, S. Yazdanfar, J. K. Barton, and A. J. Welch, "In vivo bidirectional color Doppler flow imaging of picoliter blood volumes using optical coherence tomography," Opt. Lett. **22**(18), 1439–1441 (1997).
9. J. F. de Boer, T. E. Milner, M. J. C. Van Gemert, and J. S. Nelson, "Two-dimensional birefringence imaging in biological tissue by polarization-sensitive optical coherence tomography," Opt. Lett. **22**(12), 934–936 (1997).
10. C. K. Hitzenberger, E. Götzinger, M. Sticker, and A. F. Fercher, "Measurement and imaging of birefringence and optic axis orientation by phase resolved polarization sensitive optical coherence tomography," Opt. Express **9**(13), 780–790 (2001).
11. K. Wiesauer, M. Pircher, E. Goetzinger, C. K. Hitzenberger, R. Engelke, G. Ahrens, G. Gruetzner, and D. Stifter, "Transversal ultrahigh-resolution polarization sensitive optical coherence tomography for strain mapping in materials," Opt. Express **14**(13), 5945–5953 (2006).
12. U. Morgner, W. Drexler, F. X. Kärtner, X. D. Li, C. Pitris, E. P. Ippen, and J. G. Fujimoto, "Spectroscopic optical coherence tomography," Opt. Lett. **25**(2), 111–113 (2000).
13. R. Leitgeb, M. Wojtkowski, A. Kowalczyk, C. K. Hitzenberger, M. Sticker, and A. F. Fercher, "Spectral measurement of absorption by spectroscopic frequency-domain optical coherence tomography," Opt. Lett. **25**(11), 820–822 (2000).

#159710 - $15.00 USD Received 31 Jan 2012; revised 30 Mar 2012; accepted 1 Apr 2012; published 17 Apr 2012

14. D. Adler, T. Ko, P. Herz, and J. G. Fujimoto, "Optical coherence tomography contrast enhancement using spectroscopic analysis with spectral autocorrelation," Opt. Express **12**(22), 5487–5501 (2004).
15. H. Ren, Z. Ding, Y. Zhao, J. Miao, J. S. Nelson, and Z. Chen, "Phase-resolved functional optical coherence tomography: simultaneous imaging of in situ tissue structure, blood flow velocity, standard deviation, birefringence, and Stokes vectors in human skin," Opt. Lett. **27**(19), 1702–1704 (2002).
16. B. Park, M. C. Pierce, B. Cense, S. H. Yun, M. Mujat, G. Tearney, B. Bouma, and J. de Boer, "Real-time fiber-based multi-functional spectral-domain optical coherence tomography at 1.3 μm," Opt. Express **13**(11), 3931–3944 (2005).
17. A. Dubois, L. Vabre, A. C. Boccara, and E. Beaurepaire, "High-resolution full-field optical coherence tomography with a Linnik microscope," Appl. Opt. **41**(4), 805–812 (2002).
18. L. Vabre, A. Dubois, and A. C. Boccara, "Thermal-light full-field optical coherence tomography," Opt. Lett. **27**(7), 530–532 (2002).
19. B. Laude, A. De Martino, B. Drévillon, L. Benattar, and L. Schwartz, "Full-field optical coherence tomography with thermal light," Appl. Opt. **41**(31), 6637–6645 (2002).
20. M. Akiba, K. P. Chan, and N. Tanno, "Full-field optical coherence tomography by two-dimensional heterodyne detection with a pair of CCD cameras," Opt. Lett. **28**(10), 816–818 (2003).
21. A. Dubois, G. Moneron, K. Grieve, and A. C. Boccara, "Three-dimensional cellular-level imaging using full-field optical coherence tomography," Phys. Med. Biol. **49**(7), 1227–1234 (2004).
22. W. Y. Oh, B. E. Bouma, N. Iftimia, R. Yelin, and G. J. Tearney, "Spectrally-modulated full-field optical coherence microscopy for ultrahigh-resolution endoscopic imaging," Opt. Express **14**(19), 8675–8684 (2006).
23. M. Sato, T. Nagata, T. Niizuma, L. Neagu, R. Dabu, and Y. Watanabe, "Quadrature fringes wide-field optical coherence tomography and its applications to biological tissues," Opt. Commun. **271**(2), 573–580 (2007).
24. K. Grieve, A. Dubois, M. Simonutti, M. Paques, J. Sahel, J. F. Le Gargasson, and A. C. Boccara, "In-vivo anterior segment imaging in the rat eye with high speed white light full-field optical coherence tomography," Opt. Express **13**(16), 6286–6295 (2005).
25. D. Sacchet, M. Brzezinski, J. Moreau, P. Georges, and A. Dubois, "Motion artifact suppression in full-field optical coherence tomography," Appl. Opt. **49**(9), 1480–1488 (2010).
26. A. Dubois, K. Grieve, G. Moneron, R. Lecaque, L. Vabre, and A. C. Boccara, "Ultrahigh-resolution full-field optical coherence tomography," Appl. Opt. **43**(14), 2874–2882 (2004).
27. W. Y. Oh, B. E. Bouma, N. Iftimia, S. H. Yun, R. Yelin, and G. J. Tearney, "Ultrahigh-resolution full-field optical coherence microscopy using InGaAs camera," Opt. Express **14**(2), 726–735 (2006).
28. A. Dubois, G. Moneron, and A. C. Boccara, "Thermal-light full-field optical coherence tomography in the 1.2μm wavelength region," Opt. Commun. **266**(2), 738–743 (2006).
29. D. Sacchet, J. Moreau, P. Georges, and A. Dubois, "Simultaneous dual-band ultra-high resolution full-field optical coherence tomography," Opt. Express **16**(24), 19434–19446 (2008).
30. J. Moreau, V. Loriette, and A. C. Boccara, "Full-field birefringence imaging by thermal-light polarization-sensitive optical coherence tomography I. Theory," Appl. Opt. **42**(19), 3800–3810 (2003).
31. J. Moreau, V. Loriette, and A. C. Boccara, "Full-field birefringence imaging by thermal-light polarization-sensitive optical coherence tomography II. Instrument and results," Appl. Opt. **42**(19), 3811–3818 (2003).
32. G. Moneron, A. C. Boccara, and A. Dubois, "Polarization-sensitive full-field optical coherence tomography," Opt. Lett. **32**(14), 2058–2060 (2007).
33. A. Dubois, J. Moreau, and A. C. Boccara, "Spectroscopic ultrahigh-resolution full-field optical coherence microscopy," Opt. Express **16**(21), 17082–17091 (2008).
34. S. Labiau, G. David, S. Gigan, and A. C. Boccara, "Defocus test and defocus correction in full-field optical coherence tomography," Opt. Lett. **34**(10), 1576–1578 (2009).
35. M. Laubscher, S. Bourquin, L. Froehly, B. Karamata, and T. Lasser, "Spectroscopic optical coherence tomography based on wavelength de-multiplexing and smart pixel array detection," Opt. Commun. **237**(4-6), 275–283 (2004).
36. I. Abdulhalim, R. Friedman, L. Liraz, and R. Dadon, "Full-field frequency domain common path optical coherence tomography with annular aperture," Proc. of SPIE-OSA Biomedical Optics, SPIE **6627**, 662719 (2007).
37. E. A. Swanson, D. Huang, M. R. Hee, J. G. Fujimoto, C. P. Lin, and C. A. Puliafito, "High-speed optical coherence domain reflectometry," Opt. Lett. **17**(2), 151–153 (1992).
38. M. A. Choma, M. V. Sarunic, C. H. Yang, and J. A. Izatt, "Sensitivity advantage of swept source and Fourier domain optical coherence tomography," Opt. Express **11**(18), 2183–2189 (2003).
39. R. Leitgeb, C. K. Hitzenberger, and A. F. Fercher, "Performance of fourier domain vs. time domain optical coherence tomography," Opt. Express **11**(8), 889–894 (2003).
40. W. Drexler, U. Morgner, F. X. Kärtner, C. Pitris, S. A. Boppart, X. D. Li, E. P. Ippen, and J. G. Fujimoto, "In-vivo ultrahigh-resolution optical coherence tomography," Opt. Lett. **24**(17), 1221–1223 (1999).
41. Y. Wang, Y. Zhao, J. S. Nelson, Z. Chen, and R. S. Windeler, "Ultrahigh-resolution optical coherence tomography by broadband continuum generation from a photonic crystal fiber," Opt. Lett. **28**(3), 182–184 (2003).

#159710 - $15.00 USD Received 31 Jan 2012; revised 30 Mar 2012; accepted 1 Apr 2012; published 17 Apr 2012

1. Introduction

Optical coherence tomography (OCT) is a well-established optical imaging technique with micrometer-scale resolution [1,2]. OCT is based on low-coherence interferometry to measure the intensity of light backscattered by the sample being imaged. OCT has been established in a variety of biomedical applications [3–5] and also for material characterization [6]. Several extensions of the OCT technique have been developed to provide additional imaging contrasts. By evaluating the temporal phase change of backscattered light, Doppler-OCT can identify moving particles within the sample, which enables blood flow measurements [7, 8]. Polarization-sensitive OCT takes advantage of the additional information carried by the polarization state of backscattered light to improve the imaging contrast [9–11]. Spectroscopic OCT is another technical extension that provides information on the spectral content of backscattered light by detection and processing of the whole interferometric signal [12–14]. These different extensions enable functional and structural imaging with improved differentiation between scattering structures of different types. Multimodal OCT systems have been reported, with Doppler and polarization-sensitive imaging modalities simultaneously available in addition to the conventional intensity-based mode [15, 16]. Spectroscopic OCT and polarization-sensitive OCT, on the contrary, have always been developed with distinct experimental setups. Simultaneous measurements of the spectroscopic and polarization properties of a sample with OCT have therefore never been demonstrated so far.

Full-field optical coherence tomography (FF-OCT), also referred to as full-field optical coherence microscopy (FF-OCM), is an alternative technique to OCT based on low-coherence interference microscopy [17–19]. FF-OCT produces tomographic images in the *en face* orientation by arithmetic combination of interferometric images acquired with an array camera [18–23]. The whole field to be imaged is illuminated by using a low-coherence light source (temporally and spatially) such as a light emitting diode (LED) [17], an incandescent lamp [18, 19], an arc lamp [22, 24], or a laser-pumped titanium-doped sapphire crystal [25]. Whereas conventional OCT requires scanning a light beam transversally through the sample, FF-OCT provides *en face* images without scanning. A major interest of FF-OCT lies in its ultrahigh imaging resolution in different spectral regions [26–29], far higher than the resolution of conventional OCT, using a simple and robust experimental arrangement. Two extensions to the initial FF-OCT technique were recently proposed to provide additional information on the birefringence [30–32] or spectroscopic properties [33] of the sample being imaged. These two extensions are based on distinct experimental setups. Up to now, it has therefore been impossible to measure simultaneously the birefringence properties along with the spectroscopic properties of a sample using FF-OCT.

We present in this paper a multimodal FF-OCT system, capable of measuring simultaneously the power spectrum, the intensity and the birefringence-induced phase retardation of light backscattered by the structures of a sample. The multimodal imaging technique presented here takes advantage of the high spatial resolution of FF-OCT. This paper provides a detailed description of the technique and a discussion of its features. We report on the imaging spatial resolution and discuss on the acquisition times. A theoretical analysis of the intensity detection sensitivity is carried out. The performance of this multimodal FF-OCT technique is validated by imaging a test sample presenting measurable birefringence and absorption variations in the detection spectral range. High speed imaging capability with intensity and phase retardation contrasts only is illustrated by imaging a birefringent biological tissue.

2. Experimental setup

The core of our multimodal FF-OCT system was constructed similarly to the experimental setup of polarization-sensitive FF-OCT reported in [32]. It is based on a Linnik

#159710 - $15.00 USD Received 31 Jan 2012; revised 30 Mar 2012; accepted 1 Apr 2012; published 17 Apr 2012

interferometer as depicted in Fig. 1. A 100 W tungsten halogen lamp incorporated in a Kohler illumination system provides uniform illumination with ultra-short temporal coherence. The sample to image is placed under a microscope objective in the sample arm. A reference surface is placed in the focal plane of another microscope objective located in the other arm of the interferometer. Identical water-immersion microscope objectives (Olympus, 10X, NA = 0.3) are employed to reduce dispersion mismatch between the two arms of the interferometer as the imaging depth is increased. The reference surface has a low reflectivity (R_{ref} ~2%) for optimizing the detection sensitivity as will be explained later. This low reflectivity surface is the interface between the plane surface of a polished undoped Yttrium Aluminum Garnet ($Y_3Al_5O_{12}$) crystal (refractive index of 1.82 at 750 nm) and the immersion medium. Light is linearly polarized at 0° (//) before entering the interferometer using a Glan–Thomson polarizer (Melles Griot, 03PTO105/C). An achromatic quarter-wave plate (Newport, 10RP44-2) is placed in the sample arm at 45°, so that the sample is illuminated with circularly polarized light. This ensures that the measured birefringence of the sample is independent from the optical axis orientation. Returning from the sample and passing again through the quarter-wave plate, light is in a new polarization state (elliptical in general) due to the optical anisotropy properties of the sample. Another identical achromatic quarter-wave plate is placed in the reference arm at 22.5°, so that reference light at the interferometer output is linearly polarized at a 45° angle to the incident polarization, and has equal intensity in the two orthogonal polarization states // and ⊥. A long-pass colored glass filter (Schott, RG 590) is associated to a short-pass interference filter (Thorlabs, FES1000) to reduce the width of the illumination spectrum to ~300 nm in order to fit the spectral acceptance of the wave plates. The zero-order achromatic wave plates, constructed using a stack of birefringent polymer films, provide a phase-retardation of $\pi/2$ at 720 nm with a deviation less than 1% over the wavelength range from 600 nm to 900 nm. According to the manufacturer, retardation changes are less than 1% over a ± 7° incidence angle. The maximal incidence angle in our setup being ~1°, the retardation changes are therefore much less than 1%. A broadband polarizing beam-splitter, placed at the output of the microscope, splits the interferometric image in two images with orthogonal polarizations oriented at 0° (//) and 90° (⊥) with respect to the incident polarization. These images are projected onto two identical Charge-Coupled Devices (CCD) (DALSA 1M15, 1024 × 1024 pixels, 15 Hz, 12 bits, full-well capacity of 250,000 electrons) using identical achromatic doublets with a focal length of 400 mm. 2 × 2 pixel binning is applied to increase the dynamic range of the detection, the full-well capacity of each super-pixel being then $\xi_{sat} = 10^6$ electrons. This 2 × 2 pixel binning is performed numerically after each image acquisition; the resulting images of 512 × 512 pixels are saved in 16 bit files on the computer hard disk for processing.

Unlike the polarization-sensitive FF-OCT system reported previously [32], the reference surface is here immobile and a subnanometer-resolution piezoelectric-actuated axial translation stage is used to displace the sample along the optical axis with a step of a few nanometers in order to acquire the full interferometric signal. Two stacks of interferometric images are thus acquired simultaneously by the two CCDs. After acquisition, the stacks are processed to extract the power spectrum, the intensity and the birefringence-induced phase-retardation of light backscattered by the sample. Three-dimensional images with three distinct contrasts can thus be produced. Due to the relatively long acquisition times, the interferometer is placed in a box to prevent from turbulence and the whole system is installed on an active vibration isolation table. The temperature of the room is maintained constant by air-conditioning.

If spectroscopic measurements are not desired, high-speed *en face* imaging with intensity and phase-retardation contrasts only is also possible, using fast phase-shifting interferometry by making the reference surface oscillate, as described in [32].

#159710 - $15.00 USD Received 31 Jan 2012; revised 30 Mar 2012; accepted 1 Apr 2012; published 17 Apr 2012

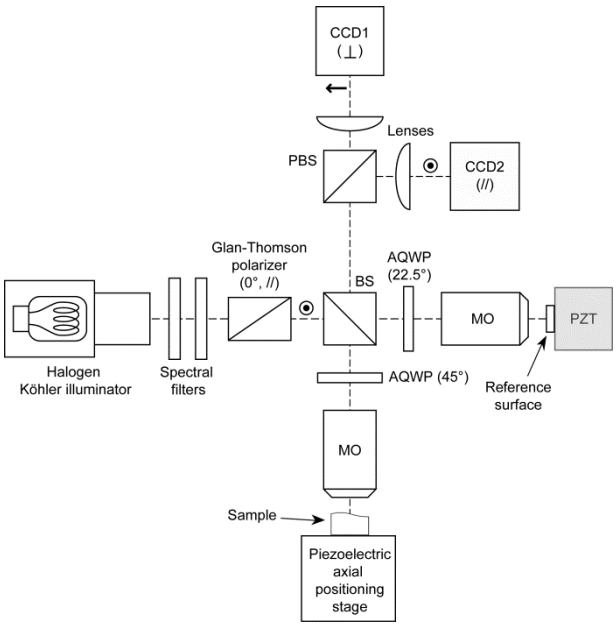

Fig. 1. Schematic of multimodal FF-OCT for simultaneous intensity, phase-retardation and power spectrum measurements. The PZT (in gray) is activated for real-time 2D *en-face* imaging (intensity and phase-retardation simultaneously). The directions of the two orthogonal linear polarization at 0° (//) and 90° (⊥) are indicated by arrows. MO: microscope objectives (water-immersion), AQWP: achromatic quarter-wave plates, BS: beam-splitter (broadband), PBS: polarizing beam-splitter (broadband).

3. Principle

The multimodal FF-OCT technique presented here is capable of simultaneous measurements of the power spectrum, the intensity and the birefringence-induced phase-retardation of light returning from the sample being imaged. The measurement procedure consists of first acquiring in parallel two stacks of interferometric images with orthogonal polarizations. The acquired interferometric data are then processed to produce images with multiple contrasts. The principle of these measurements is described in this section.

3.1 Acquisition of the interferometric data

The sample is displaced, using the high-resolution piezoelectric stage, in the axial direction in steps small enough to resolve the interference fringes. The displacement increment is adjusted to a value of δ = 35 nm, which corresponds to a phase change in the interferometer of $4\pi \times n_{im} \times \delta / \lambda \sim \pi/4$, where n_{im} is the refractive index of the objective immersion medium and λ = 750 nm is the central wavelength of the detected signal. The interferometric signal is thus acquired with a sampling rate about four times above the Nyquist limit. At each step k, a number N_{acc} of images are acquired by each CCD and are summed up in order to increase the dynamic range and hence the detection sensitivity as will be explained later. The resulting two interferometric images with orthogonal polarizations are saved on the computer hard disk.

The numbers of photo-electrons delivered by each pixel of coordinates (n_x, n_y) of CCD1 ($\perp$) and CCD2 (//), at step k after accumulation of N_{acc} images are, respectively:

#159710 - $15.00 USD Received 31 Jan 2012; revised 30 Mar 2012; accepted 1 Apr 2012; published 17 Apr 2012

$$E_k^{\perp}(n_x,n_y)=\eta\left\{R_{inc}^{\perp}(x,y)+R_{sample}^{\perp}(x,y,z)+R_{ref}^{\perp}+2\sqrt{R_{sample}^{\perp}(x,y,z)R_{ref}^{\perp}}\cos\left[\varphi^{\perp}(x,y,z)+k\frac{\pi}{4}\right]\right\},\tag{1.a}$$

and

$$E_k^{//}(n_x,n_y)=\eta\left\{R_{inc}^{//}(x,y)+R_{sample}^{//}(x,y,z)+R_{ref}^{//}+2\sqrt{R_{sample}^{//}(x,y,z)R_{ref}^{//}}\cos\left[\varphi^{//}(x,y,z)+k\frac{\pi}{4}\right]\right\}.\tag{1.b}$$

The proportionality constant $\eta = N_{acc}\gamma sTI_0/8$ includes the number of accumulated images N_{acc}, the CCD quantum efficiency γ, the CCD pixel surface s, the CCD integration time T, and the irradiance (sometimes called intensity) I_0 of light at the interferometer entrance before passing through the polarizer. The spatial coordinates (x, y, $z = k\delta$) locate a point in the coherence plane with transverse coordinates (x, y) after axial displacement of the sample by a distance $z = k\delta$. The image of this point on the CCD arrays is centered about the CCD pixels of coordinates (n_x, n_y). By definition, the coherence plane is the plane in the sample arm orthogonal to the optical axis, and located at the same optical distance from the interferometer beam splitter than the reference surface. The coherence plane perfectly coincides with the focal plane of the microscope objective when the surface of the sample is imaged. These two planes separate from each other as the imaging depth increases, all the more than the refractive index of the sample differs from the refractive index of the immersion medium [28]. When dry microscope objectives are used, this effect has to be corrected otherwise the accessible imaging depth may be very limited [34]. Here, such a correction is not required since we use water as immersion medium to minimize the refractive index mismatch with the sample, and a relatively low numerical aperture (NA = 0.3). The interference with light backscattered by a structure in the sample has a maximal contrast when the structure is located in the coherence plane. The contrast drops when the distance of the structure from the coherence plane increases. The contrast drop is described by the so-called coherence envelope. A coherence slice can be defined as a slice of width equal to the coherence length (width of the coherence envelope) centered about the coherence plane. In the mathematical description used here, instead of introducing a coherence envelope, we consider that light returning from the sample and collected by the microscope objective can be decomposed into two parts depending on whether it originates from the coherence slice or not. Light backscattered by the sample structures in the coherence slice is regarded as if it originates from a surface with reflectivity distribution $R_{sample}(x, y)$ located in the coherence plane. This component of light interferes with light reflected by the reference surface. When the axial position of the sample is varied, the reflectivity distribution $R_{sample}(x, y)$ changes since different structures of the sample are in the coherence slice. That is why the notation $R_{sample}(x, y, k\delta)$ is used in the equations. Light backscattered by the sample structures present outside the coherence slice does not interfere. The proportion of this light collected by the microscope objective is represented by an equivalent reflectivity R_{inc}. This quantity, made up from all reflected and backscattered components throughout the sample except those in the coherence slice, can be considered as independent of the sample axial position. The reflection coefficients R_{sample} and R_{inc}, as well as the reflection coefficient of the reference surface R_{ref}, are separated into two components concerning light with $\perp$ or // polarizations (detected by CCD1 or CCD2, respectively). They are denoted as $R_{sample}^{\perp}$, $R_{sample}^{//}$, $R_{inc}^{\perp}$, $R_{inc}^{//}$, $R_{ref}^{\perp}$ and $R_{ref}^{//}$. We obviously have $R_{sample} = R_{sample}^{\perp} + R_{sample}^{//}$, $R_{inc} = R_{inc}^{\perp} + R_{inc}^{//}$, and $R_{ref} = R_{ref}^{\perp} + R_{ref}^{//}$. Due to the short coherence length of the light source, the proportion of light returning from

#159710 - $15.00 USD Received 31 Jan 2012; revised 30 Mar 2012; accepted 1 Apr 2012; published 17 Apr 2012

the sample that interfere is small compared to the proportion of light that does not interfere, *i.e.* $R^{\perp}_{sample}(x,y,z) \ll R^{\perp}_{inc}(x,y)$ and $R^{//}_{sample}(x,y,z) \ll R^{//}_{inc}(x,y)$. We can also assume that $R_{sample}(x,y,z) \ll R_{ref}(x,y)$. Finally, it is obvious that $R^{\perp}_{ref} = R^{//}_{ref} = R_{ref}/2$ (~1%).

Using the Jones matrix formalism, we can establish that the sample reflectivity R_{sample} (structures located in the coherence slice) and the optical phase φ in the interferometer satisfy the following equations [9, 10]:

$$\begin{cases} R^{\perp}_{sample} = R_{sample}\cos^2\phi \\ R^{//}_{sample} = R_{sample}\sin^2\phi \end{cases}, \tag{2}$$

and

$$\begin{cases} \varphi^{\perp} = \varphi \\ \varphi^{//} = \varphi + 2\alpha \end{cases}, \tag{3}$$

where ϕ denotes the single-pass phase-retardation, and α the angle with the // direction (see Fig. 1) of the fast optical axis of the birefringent sample. Taking into account the notations and the different assumptions seen previously, we can write simplified expressions for the number of photo-electrons delivered by each pixel of coordinates (n_x, n_y) of both cameras at each step *k*:

$$E^{\perp}_k = \eta\left\{R^{\perp}_{inc} + \frac{R_{ref}}{2} + 2\sqrt{R_{sample}\frac{R_{ref}}{2}}\cos\phi\cos\left[\varphi + k\frac{\pi}{4}\right]\right\}, \tag{4.a}$$

$$E^{//}_k = \eta\left\{R^{//}_{inc} + \frac{R_{ref}}{2} + 2\sqrt{R_{sample}\frac{R_{ref}}{2}}\sin\phi\cos\left[\varphi + 2\alpha + k\frac{\pi}{4}\right]\right\}. \tag{4.b}$$

3.2 Calculation of the spectroscopic information

Power spectra of light emanating from distinct points in the sample imaged by an OCT system can be obtained by Fourier analysis of the detected interferometric signal [12]. A similar approach can be applied in FF-OCT [33]. It has to be noted, however, that the spectral information measured at an arbitrary depth in the sample where scattering occurs is not strictly spatially-resolved since it results from the effects of absorption and scattering of light during its propagation from the surface to this depth and back to the surface.

Pseudo spatially-resolved power spectra are obtained with our FF-OCT system by Fourier analysis of the data acquired by CCD1, *i.e.* a *z*-stack of *N* interferometric images ($k = 0, 1, \ldots, N$) of 512 × 512 points, each of them being the sum of N_{acc} images at the same position. In practice, N_{acc} ~10 and 1,000 < *N* <15,000 (scanned depth between 35 µm and 500 µm). For each value of the camera pixel coordinates (n_x, n_y), the vector $E^{\perp}(n_x, n_y)$ of *N* points is multiplied by a Gaussian function whose peak position is varied. This function is also a vector of *N* points. The Fast Fourier Transform (FFT) of the resulting vector is then calculated. The FFT calculation is repeated *N* times, the center of the Gaussian function being shifted by one point between successive FFT calculations. *N* spatially-resolved spectra are thus obtained. This procedure is repeated for all values of (n_x, n_y) (*i.e.*512 × 512 times). 512 × 512 × *N* spectra are finally obtained, each of them being associated to one point of the three-dimensional data set $E^{\perp}$. If *N* < 4096, zero-padding is applied before calculating the FFT in order to reduce the spectrum sampling step, which is therefore at

#159710 - $15.00 USD Received 31 Jan 2012; revised 30 Mar 2012; accepted 1 Apr 2012; published 17 Apr 2012

least $\delta\sigma = \left(2 \times 4096 \times \delta z\right)^{-1}$ = 35 cm^{-1} (~2 nm at λ = 750 nm). The choice of the Gaussian window size to calculate the FFT results in a trade-off between the spectral resolution and the spatial resolution of the spectral data. A narrow Gaussian window was chosen, with width equal to the imaging axial resolution, *i.e.* a full width at half maximum (FWHM) of 1.0 µm, which corresponds to 30 points. The spectral impulse response being the Fourier transform of this Gaussian window, the spectral resolution, defined as the FWHM of the spectral impulse response, is therefore equal to 240 nm. Despite a low spectral resolution, spectral shifts can be measured with a sensitivity of a few nanometers on an immobile sample depending on the signal-to-noise ratio [33]. These spectral shifts can be localized with a spatial resolution of ~1 µm. After a local spectrum has been calculated for each point of the imaged volume, it is necessary to quantify some aspect of the spectra for display. Due to the low spectral resolution, spectral modulations due to interference are not resolved; the measured spectra are always peak functions. An appropriate spectroscopic metric is then the spectrum center of mass. We can thus obtain and display the mean wavelength of detected light that is backscattered at each point of the volume being imaged in the sample.

Alternative methods for accessing spectroscopic information in FF-OCT without post-processing, based on wavelength de-multiplexing and parallel detection, have been demonstrated or suggested [35, 36]. Comparatively, these methods are insensitive to scan non-linearities or sample movements and can therefore potentially provide better sensitivity and accuracy since they are faster. They are however technically more difficult to implement. On the contrary, the application of Fourier-transform spectroscopy in OCT (including FF-OCT) is straightforward since OCT is based on a Michelson-type interferometer.

3.3 Calculation of intensity and phase-retardation

Intensity and phase-retardation are extracted from the stack of interferometric images acquired by both cameras. The method is based on phase-shifting interferometry. It consists of combining several interferometric images presenting a relative phase-shift. We use here an algorithm with four interferometric images with a phase-shift of $\pi/2$ between successive images. Since successive images in the stack have a phase difference of $\pi/4$, we consider every other image of the stack in the following image combinations:

$$\begin{cases} C_k^{\perp} = \left(E_k^{\perp} - E_{k+4}^{\perp}\right)^2 + \left(E_{k+2}^{\perp} - E_{k+6}^{\perp}\right)^2 \\ C_k^{//} = \left(E_k^{//} - E_{k+4}^{//}\right)^2 + \left(E_{k+2}^{//} - E_{k+6}^{//}\right)^2 \end{cases}. \tag{5}$$

By calculating the sum

$$C_k^{\perp}(n_x, n_y) + C_k^{//}(n_x, n_y) = \left(\frac{N_{acc}\gamma s T I_0}{2\sqrt{2}}\right)^2 R_{ref} R_{sample}(x, y, z = k\delta), \tag{6}$$

we obtain a quantity proportional to $R_{sample}(z = k\delta)$, which represents the distribution of the intensity of light backscattered by the sample structures located in the coherence slice as a function of the sample axial position $z = k\delta$, *i.e.* an *en face* intensity-based tomographic image. A stack of (N-6) such tomographic images is calculated by applying Eq. (6) for all the values of the index k. Successive images in the stack correspond to depth difference of δ = 35 nm.

The ratio

$$\frac{C_k^{//}(n_x, n_y)}{C_k^{\perp}(n_x, n_y)} = \tan^2 \phi(x, y, z = k\delta) \tag{7}$$

#159710 - $15.00 USD Received 31 Jan 2012; revised 30 Mar 2012; accepted 1 Apr 2012; published 17 Apr 2012

gives access to the quantity $\phi(z = k\delta)$, which represents the phase-retardation of light backscattered by the sample structures located in the coherence slice for an axial position of the sample $z = k\delta$. It has to be noted that this measured phase-retardation results from the accumulation of phase changes occurring during the propagation of light in the sample from the surface to the imaging depth and back to the surface. By applying Eq. (7) for all the values of the index k, a stack of (N-6) *en face* phase-retardation images is calculated.

The previous equations were established by assuming that $R_{sample}(x, y, z = k\delta)$, $\varphi(x, y, z = k\delta)$ and $\alpha(x, y, z = k\delta)$ are constant in the four interferometric images used for the calculations. This assumption is valid since the total axial displacement of the sample required in the four-frame algorithm is 6δ = 210 nm, which is much less than the coherence length.

4. Performance

We propose in this section to establish an expression of the intensity detection sensitivity of our imaging system. This parameter is of particular importance, because it often determines the maximal imaging depth in scattering samples. The case of the imaging of a non birefringent sample is treated separately since only one camera is then required. We also report on the spatial resolution of the system. At last, we discuss acquisition times.

4.1 Intensity detection sensitivity

When no interference is detected, the intensity-based tomographic image has a mean value that corresponds to the background level. In the absence of noise, the background level would be zero (see Eq. (6), when $R_{sample} = 0$). In reality, the background level is not zero because of the presence of noise. Since only a signal greater than the background level can be detected, this level corresponds to the signal generated by the smallest detectable reflectivity defined as the intensity detection sensitivity of our imaging system. We assume that the predominant noise results from the shot-noise (this assumption will be justified later). Ordinarily this noise is Poisson distributed, implying that the variance of the number of photo-electrons stored by each CCD pixel is equal to the number of photo-electrons itself. We model the shot-noise as an additive component v superimposed to the signal delivered by the CCD pixels of both cameras. This noise has the following properties:

$$\begin{cases} \left\langle v^{\perp} \right\rangle = \left\langle v^{//} \right\rangle = 0 \\ \left\langle \left(v^{\perp}\right)^2 \right\rangle = \sigma_{\perp}^2 \\ \left\langle \left(v^{//}\right)^2 \right\rangle = \sigma_{//}^2 \\ \left\langle v_i^{\perp} v_j^{\perp} \right\rangle = \left\langle v_i^{//} v_j^{//} \right\rangle = 0 \quad i \neq j, \end{cases} \tag{8}$$

where the angular brackets denote a time average. In the presence of noise, the image combinations expressed in Eq. (5) should be rewritten as

$$\begin{cases} C_{\mathrm{k}}^{\perp} = \left[\left(E_k^{\perp} + v_k^{\perp}\right) - \left(E_{k+4}^{\perp} + v_{k+4}^{\perp}\right)\right]^2 + \left[\left(E_{k+2}^{\perp} + v_{k+2}^{\perp}\right) - \left(E_{k+6}^{\perp} + v_{k+6}^{\perp}\right)\right]^2 \\ C_{\mathrm{k}}^{//} = \left[\left(E_k^{//} + v_k^{//}\right) - \left(E_{k+4}^{//} + v_{k+4}^{//}\right)\right]^2 + \left[\left(E_{k+2}^{//} + v_{k+2}^{//}\right) - \left(E_{k+6}^{//} + v_{k+6}^{//}\right)\right]^2 \end{cases}. \tag{9}$$

The illumination power is adjusted so that the number of photo-electrons delivered by each CCD pixel of both cameras is close to the full-well capacity ξ_{sat}. If the sample is birefringent,

#159710 - $15.00 USD Received 31 Jan 2012; revised 30 Mar 2012; accepted 1 Apr 2012; published 17 Apr 2012

we may assume that $R_{inc}^{\perp} = R_{inc}^{//} = R_{inc}/2$. Since $R_{sample} \ll R_{ref}$, we can write, according to Eqs. (4), that

$$\xi_{sat} \sim \frac{\gamma s T I_0}{16}\left(R_{ref} + R_{inc}\right). \tag{10}$$

The intensity background level is given by the average value of $C_k^{\perp} + C_k^{//}$, when $R_{sample}^{\perp} = R_{sample}^{//} = 0$, *i.e.*

$$\left\langle \left(\nu_k^{\perp} - \nu_{k+4}^{\perp}\right)^2 + \left(\nu_{k+2}^{\perp} - \nu_{k+6}^{\perp}\right)^2 + \left(\nu_k^{//} - \nu_{k+4}^{//}\right)^2 + \left(\nu_{k+2}^{//} - \nu_{k+6}^{//}\right)^2 \right\rangle = 4\left(\sigma_{\perp}^2 + \sigma_{//}^2\right)$$
$$= \left(\frac{N_{acc}\gamma s T I_0}{2\sqrt{2}}\right)^2 R_{ref} R_{min}, \tag{11}$$

where R_{min} denotes the smallest detectable reflectivity. The variance of the shot-noise for both cameras being $\sigma_{\perp}^2 \sim \sigma_{//}^2 \sim N_{acc}\xi_{sat}$, we establish by combining Eqs. (10) and (11) that

$$R_{min} = \frac{\left(R_{ref} + R_{inc}\right)^2}{4 N_{acc} \xi_{sat} R_{ref}}. \tag{12}$$

Equation (12) shows the influence of several parameters on the detection sensitivity. A full-well capacity ξ_{sat} as large as possible is desirable, this value being multiplied by the number N_{acc} of images that are accumulated. The equivalent reflection coefficient R_{inc} must be as low as possible, but cannot be really controlled since it is determined mainly by the sample itself. By calculating the derivative of Eq. (12) with respect to R_{ref}, one can see that the optimal reflectivity of the reference surface is $R_{ref} = R_{inc}$. This optimal value therefore depends on the sample being imaged, but does not exceed a few percents for most biological tissues. Equation (12) shows that a detection sensitivity $-10 \times \log(R_{min})$ on the order 90 dB can be obtained with our imaging system in an acquisition time of ~3 s ($R_{ref} = 0.02$, $R_{inc} = 0.01$, $N_{acc} = 10$, $\xi_{sat} = 10^6$). This means that a reflectivity as low as $R_{min} = 10^{-9}$ can be detected.

A particularly interesting feature of FF-OCT is that the detection sensitivity does not depend on the illumination bandwidth. This is an advantage over time-domain scanning OCT, where detection sensitivity and illumination bandwidth are inversely proportional [37]. In frequency-domain OCT, the illumination bandwidth does not affect the detection sensitivity as well [38]. This latter technique achieves the best trade-off between detection sensitivity and acquisition speed along with high axial resolution [39]. On the other hand, the transverse resolution of frequency-domain OCT is limited to 10-20 µm, which is one order of magnitude larger than the transverse resolution that can be achieved with FF-OCT as will be shown.

4.2 Imaging of a non-birefringent sample

If the sample being imaged is not birefringent, CCD2 does not receive any light from the sample ($R_{sample}^{//} = R_{inc}^{//} = 0$). In that case, one stack of interferometric images is acquired by CCD1 only and processed to obtain spectroscopic and intensity information. Since $C_k^{//} = 0$, the intensity-based images are then calculated from the image combination $C_k^{\perp}$. Let us calculate the detection sensitivity in that case. We have

#159710 - $15.00 USD Received 31 Jan 2012; revised 30 Mar 2012; accepted 1 Apr 2012; published 17 Apr 2012

$$C_k^{\perp}(n_x, n_y) = \left(\frac{N_{acc} \gamma s T I_0}{2\sqrt{2}} \right)^2 R_{ref} R_{sample}(x, y, z = k\delta), \tag{13}$$

and

$$\xi_{sat} \sim \frac{\gamma s T I_0}{8} \left(R_{ref} / 2 + R_{inc} \right). \tag{14}$$

When $R_{sample} = 0$, the average value of $C_k^{\perp}$ is

$$\left\langle C_k^{\perp} \right\rangle = \left\langle \left(\nu_k^{\perp} - \nu_{k+4}^{\perp} \right)^2 + \left(\nu_{k+2}^{\perp} - \nu_{k+6}^{\perp} \right)^2 \right\rangle = 4\sigma_{\perp}^2 \sim 4 N_{acc} \xi_{sat}. \tag{15}$$

From Eqs. (13), (14) and (15), the expression of the lowest detectable reflectivity can be derived:

$$R_{min} = \frac{\left(R_{ref} / 2 + R_{inc} \right)^2}{2 N_{acc} \xi_{sat} R_{ref}}. \tag{16}$$

The optimal reflectivity of the reference surface, calculated by considering the derivative of Eq. (16) with respect to R_{ref}, is then $R_{ref} = 2\, R_{inc}$.

In order to check the validity of our theoretical analysis, the lowest detectable reflectivity R_{min} was measured using a BK7-glass prism as a sample, providing a reflectivity of $R_{sample} = \left[\left(n_{im} - n_{glass} \right) / \left(n_{im} + n_{glass} \right) \right]^2 = 0.4\%$ at the interface glass/water. Due to the angle of the prism, light reflected by the lower surfaces was not collected by the microscope objective. A stack of tomographic images was acquired by translating the sample in 35 nm steps using the high-resolution piezoelectric-actuated axial translation stage. The variation of the signal $C_k^{\perp}(256, 256)$, corresponding to the intensity at the center of the tomographic images ($n_x = n_y = 256$), is represented in Fig. 2 in logarithmic scale, as a function of the sample axial position. The signal was calibrated in reflectivity units, since $C_k^{\perp}$ is proportional to R_{sample} and $10 \times \log R_{sample}(z = 0) = -24$ dB. The signal drops when the sample surface moves away from the coherence plane (located at $z = 0$). Weak side lobes can be observed resulting from the shape of the detected light spectrum which is not ideally Gaussian. Far enough from the coherence plane, the signal reaches a constant average value of −94 dB, which corresponds to the background noise of the system. The minimal detectable reflectivity R_{min} is identified to this value. The calculation of R_{min} using Eq. (16) with the experimental parameters ($N_{acc} = 10$, $\xi_{sat} = 10^6$, $R_{ref} = 2\%$, and $R_{inc} = 0.2\%$) gives −94.4 dB. The measurements confirm the validity of the theoretical analysis and the assumption of a shot-noise limited detection.

#159710 - $15.00 USD Received 31 Jan 2012; revised 30 Mar 2012; accepted 1 Apr 2012; published 17 Apr 2012

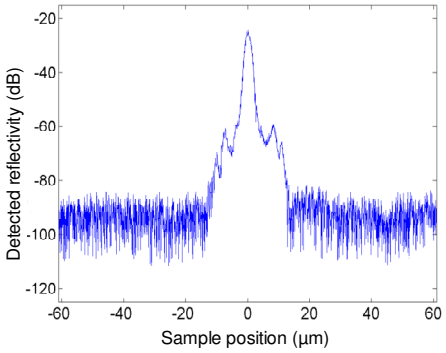

Fig. 2. Axial response of the FF-OCT system in logarithmic scale. Glass was used as a low reflectivity (−24 dB) sample scanned through the focus of the objective.

4.3 Spatial resolution

The spatial resolution of an imaging system can be characterized by the image of a point, *i.e.* the so-called point-spread function (PSF). In FF-OCT, the PSF is determined by the properties of both the microscope objectives and the power spectrum of the detected light.

In the transverse direction (plane orthogonal to the optical axis of the microscope objectives), the theoretical diffraction-limited PSF of FF-OCT is identical to the one of confocal microscopy [17]. It is described by the squared Airy function

$$I(r) = \left[\frac{2J_1\left(2\pi rNA/\lambda\right)}{2\pi rNA/\lambda} \right]^4. \tag{17}$$

The diffraction-limited transverse resolution can be defined as the FWHM of this function, *i.e.*

$$\Delta r \sim \frac{0.37\lambda}{NA}. \tag{18}$$

The theoretical transverse resolution of FF-OCT depends on the center optical wavelength λ and the numerical aperture *NA* of the microscope objectives. The effective center wavelength being λ = 750 nm, the theoretical transverse resolution, at the surface of the sample, is therefore ~1 µm when microscope objectives with numerical aperture of 0.3 are employed. We mention that a degradation of the resolution occurs progressively when the imaging depth increases due to refractive index mismatch between the sample and the immersion medium. This effect is common to all microscopy systems and may become dramatic when a high numerical aperture is employed. In comparison, the transverse resolution of conventional OCT is 10-20 times lower since this technique produces B-scans (obtained images are in a plane parallel to the optical axis), which requires a depth of focus equal to the axial extent of the images and therefore a low numerical aperture.

The axial resolution of FF-OCT is determined theoretically by both the effective coherence length and the depth of focus of the microscope objectives [17]. The FWHM of the axial response, at the surface of the sample, is given by

$$\Delta z = \left[\frac{NA^2}{n_{im}\lambda} + \frac{n_{im}\pi}{2\ln 2}\left(\frac{\Delta\lambda}{\lambda^2}\right) \right]^{-1}, \tag{19}$$

where n_{im} is the refractive index of the objective immersion medium and $\Delta\lambda$ the effective source spectral bandwidth. With our filtered halogen lamp, the axial resolution is imposed by

#159710 - $15.00 USD Received 31 Jan 2012; revised 30 Mar 2012; accepted 1 Apr 2012; published 17 Apr 2012

the coherence length to ~1 µm. This ultrahigh axial resolution also degrades with the imaging depth due to dispersion mismatch between the interferometer arms, although this mismatch is minimized by using water-immersion microscope objectives. In comparison with ultra-short femtosecond lasers or supercontinuum fiber lasers used for ultrahigh-resolution OCT [40, 41], a thermal light source has a smoother spectrum that does not contain spikes or emission lines that could cause side lobes in the coherence function and create artifacts in the images.

4.4 Acquisition times

In order to make spectroscopic measurements, two stacks of interferometric images need to be acquired with a step small enough to resolve the interference fringes. Considering the number of fringes to be resolved to produce one single *en-face* spectroscopic image to be equal to twice the FWHM of the Gaussian window (1.0 µm) divided by the sampling step (35 nm), it is necessary to acquire $2 \times N_{acc} \times (1000/35)$ images, which represents a time of ~45 s with our camera (frame rate of 15 Hz, with N_{acc} = 10). In practice, we scan the entire accessible imaging depth of the sample. For example, the acquisition of two stacks of accumulated interferometric images (N_{acc} = 10) from the surface of the sample down to a depth of 200 µm represents an acquisition time of about 70 min. This long acquisition time is limited by the CCD frame rate and full-well-capacity, and also by the time spent accessing and writing the data on the computer hard disk. Because of the acquisition time, the technique is currently not suitable for *in vivo* imaging, and care must also be taken to avoid mechanical instabilities in the interferometer. Other approaches for accessing spectroscopic information, based on wavelength de-multiplexing and parallel detection [35, 36], are much faster than the Fourier-analysis method used here. These approaches therefore require less care for mechanical and thermal stability and are more appropriate for *in vivo* applications. Their implementation in FF-OCT is however not so straightforward. We can reasonably expect to reduce the acquisition time of our FF-OCT system by a factor of at least ten by using the latest generations of high dynamic CMOS cameras and fast computers. Appropriate cameras would be characterized by a higher value of the product $\xi_{sat} \times f_{frame}$ where ξ_{sat} and f_{frame} denote the full-well capacity and the frame rate, respectively. One single *en face* spectroscopic image would then be obtained in a few seconds.

If spectroscopic measurements are not desirable, it is possible to obtain intensity and phase-retardation in a much shorter time, since it is not necessary to acquire the full interferometric signal, *i.e.* to resolve the interference fringes. Only the amplitude of the interference signal in two orthogonal polarization states needs to be measured. Theoretically, three pairs of interferometric images (*i.e.* 6 images) are enough to calculate an *en face* image with intensity and phase-retardation information. In practice, we use a combination of 4 pairs of interferometric images (*i.e.* a total of 8 images; each camera acquires 4 images), the phase being shifted in the interferometer between each image pair acquisition, as explained in [32]. The phase-shift is achieved by making the reference mirror oscillate, using a piezoelectric actuator (see Fig. 1), at a frequency equals to one quarter of the CCD frame rate (*i.e.* 3.75 Hz). The CCD cameras are synchronized with the PZT oscillation to acquire 4 images per modulation period. With our cameras, the acquisition time to produce an *en face* image with both intensity contrast and phase-retardation contrast is about 3 seconds (with N_{acc} = 10). For the same detection sensitivity, this time could even be reduced by using cameras so that the product $\xi_{sat} \times f_{frame}$ is higher. The decrease in acquisition time would then be inversely proportional to the increase of this product, provided that the cameras still operate close to the shot-noise limit.

#159710 - $15.00 USD Received 31 Jan 2012; revised 30 Mar 2012; accepted 1 Apr 2012; published 17 Apr 2012

5. Multimodal imaging capability

5.1 Validation of combined intensity/spectroscopic/phase-retardation imaging

In order to demonstrate the capability of our imaging system to measure simultaneously the intensity, the power spectrum and the phase-retardation of light backscattered by the sample being imaged, we tried to find a sample presenting both birefringence and absorption variations in the detection spectral region, *i.e.* between 500 nm and 1000 nm. We used an infrared viewing card (Thorlabs, model VRC5) as a test sample. This card is characterized by a spectral sensitivity in the range between 700 nm and 1400 nm, with a maximum of sensitivity around 1000 nm. The absorption of the phosphore-based photosensitive material, strictly increasing with wavelength in the imaging band, is therefore expected to modify the power spectrum of light having travelled a certain distance through the photosensitive material. This photosensitive material is encapsulated between two plastic layers. Since many plastic materials are birefringent, we also expect to detect phase-retardation changes of backscattered light emanating from the sample.

A stack of N = 12,800 accumulated interferometric images was acquired and processed. Figure 3 shows three xz-oriented sections with intensity-based contrast (a), spectroscopic contrast (b) and phase-retardation contrast (c).

The intensity-based image (Fig. 3(a)) reveals part of the internal structure of the viewing card. Three distinct layers can be distinguished. The upper layer corresponds to plastic material with a thickness of 170 µm. A random distribution of scattering structures is revealed inside this polymer material. The bottom layer, very inhomogeneous, corresponds to the photosensitive material. The middle layer, in contrast, is very homogeneous since no scattered light is detected from this region. This layer is assumed to be the glue used for maintaining the photosensitive material attached to the plastic layers.

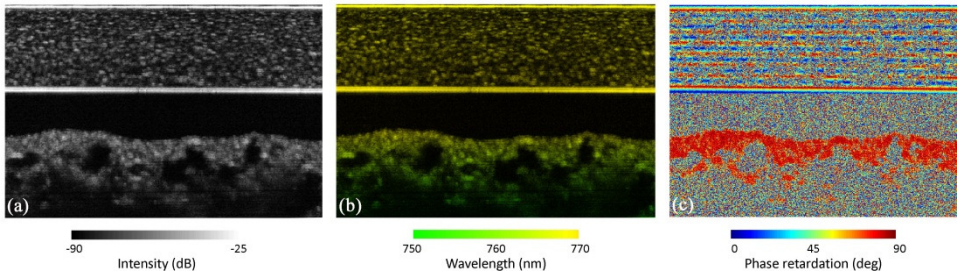

Fig. 3. Cross-sectional multimodal FF-OCT images of an infrared viewing card. Intensity-based image (a), spectroscopic image (b), and phase-retardation image (c). The size of each image is 650 µm (x) × 450 µm (z).

The spectroscopic image (Fig. 3(b)) is actually a combination of spectroscopic and intensity measurements displayed using a hue/saturation/luminance (HSL) color map. Hue encodes the spectroscopic information, *i.e.* the center of mass of the spatially-resolved spectra, whereas luminance encodes the intensity information. Hue variation is restricted in the range from 56° to 117°, whereas luminance ranges from 0 to 1. The saturation parameter is set to 1. A shift of the spectrum center of mass of light emanating from the photosensitive material towards shorter wavelengths is observed as depth increases. The maximal value of the detected spectral shifts reaches 18 nm. In order to verify the validity of this result, the viewing card was placed in front of the halogen lamp and the spectrum of light transmitted by the card was measured using a silicon-based spectrometer (Ocean Optics, HR4000). Figure 4(a) compares this measured spectrum with the spectrum measured without the card in front of the lamp. We can see the effect of the photosensitive material which attenuates more the long wavelengths than the short wavelengths in the spectrometer detection band. The

#159710 - $15.00 USD Received 31 Jan 2012; revised 30 Mar 2012; accepted 1 Apr 2012; published 17 Apr 2012

centers of mass of these two spectra are calculated over the wavelength range 670 nm – 1000 nm. They are located at 865 nm and 888 nm for the transmitted and incident light, respectively. The corresponding spectral shift of 23 nm is consistent with the measurements provided by the spectroscopic modality of the FF-OCT system.

Figure 3(c) shows an image reconstructed from polarization-sensitive measurements. The phase-retardation is coded with a color map varying from blue (0 degrees) to red (90 degrees). Fringes parallel to the surface are observed in the superficial layer with a constant period of p = 25 ± 2 µm. This reveals a homogeneous birefringence of this layer made of plastic. The value of the birefringence can be deduced from $\delta n = \lambda/(4p)$ = 0.007 ± 0.001, λ being the mean wavelength (750 nm). Birefringence is common in plastic materials because their molecules are frozen in a stretched conformation when the plastic is molded. The birefringence of the intermediate layer cannot be measured since no backscattered light is detected from this region. The lower layer, corresponding to the photosensitive material, does not exhibit any measurable birefringence. In order to check the estimated value of the birefringence of the plastic layer, we removed this layer from the card and measured its birefringence using a conventional method of spectral modulation (see Fig. 4(b)). The sample was placed between two crossed polarizers oriented at 45° with respect to its optical axis found by rotating the sample. The spectrum of light at the output was measured using the Ocean Optics spectrometer and was fitted with the theoretical spectrum

$$I(\lambda) = S(\lambda) \times \left[1 - \alpha \cos\left(2\pi \times \delta n \times e / \lambda\right)\right] / 2. \qquad (20)$$

The fitting parameters were the birefringence δn and the fringe contrast α. $S(\lambda)$ was the measured spectrum emitted by the lamp and e the thickness of the sample measured by interferometry to be 170 µm. The fitting procedure gave a birefringence value δn = 0.0057, which is in concert with the value obtained from the polarization-sensitive modality of the FF-OCT system.

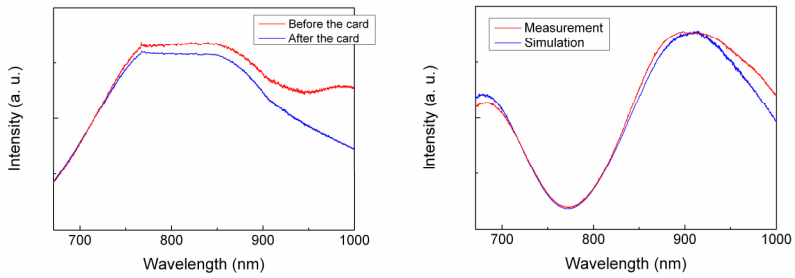

(a) (b)

Fig. 4. (a) Normalized spectra of light emitted by the halogen lamp before and after passing through the infrared viewing card. (b) Measured and simulated spectra of light emitted by the halogen lamp after passing through the upper plastic layer of the viewing card placed between crossed polarizers.

5.2 Illustration of high-speed intensity/phase-retardation imaging

To demonstrate the capability of our FF-OCM system for high-speed imaging with both intensity and phase-retardation contrasts acquired simultaneously, we propose to show images of a birefringent biological tissue. A piece of muscle tissue was excised from a shrimp tail and imaged. Figure 5 shows a pair of *en-face* (*xy*) images acquired at a depth of 50 µm below the sample surface. The acquisition time of this image pair was ~3 seconds, due to an accumulation of 10 interferometric images. The contrasts in the intensity and phase images are different and uncorrelated, since they result from distinct physical mechanisms. The phase image (Fig. 5(b)) reveals optical anisotropy inhomogeneities in the tissue that are

#159710 - $15.00 USD Received 31 Jan 2012; revised 30 Mar 2012; accepted 1 Apr 2012; published 17 Apr 2012

invisible in the intensity image. On the other hand, the intensity image (Fig. 5(a)) reveals the presence of scattering structures that do not appear in the phase image.

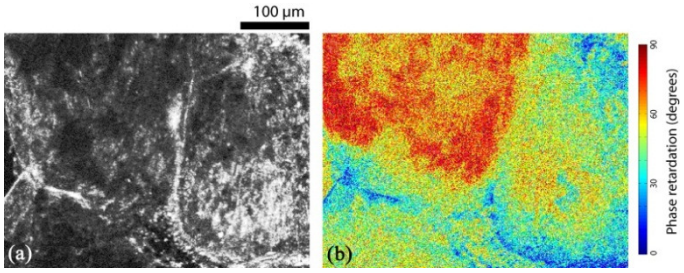

Fig. 5. *En-face* intensity (a) and phase-retardation (b) images of shrimp muscle at an average depth of 50 µm below the surface.

6. Conclusions

A FF-OCT system capable of producing images with multiple contrasts was demonstrated. The acquired data can be processed to display simultaneously the intensity, the power spectrum, and the phase-retardation of light backscattered by the sample being imaged. All these imaging modalities had never been available simultaneously using a single FF-OCT system or even a single conventional OCT system. The multimodal imaging technique presented here offers an isotropic ultrahigh spatial resolution of ~1 µm, by using a simple tungsten halogen lamp. With a moderate increase in experimental setup complexity and cost compared to conventional FF-OCT, extended imaging capabilities are achieved, thus making it easier to differentiate between backscattering structures within the sample.

Acknowledgments

This work would not have been possible without the invaluable contribution of postdoctoral associates and PhD students, including Gael Moneron, Julien Moreau, and Delphine Sacchet. I am particularly grateful to Claude Boccara, Professor of Optical Sciences at the École Supérieure de Physique et de Chimie Industrielles de la ville de Paris for our impassioned discussions and to Patrick Georges, my colleague at Institut d'Optique. We acknowledge support from the European network Photonics4Life.